Journal of Information Systems Engineering and Management
2024, 9(4s)
e-ISSN: 2468-4376
https://www.jisem-journal.com/ **Research Article**

Residue Learning Deep Discriminative Network for 3D Magnetic Resonance Image Denoising and Bias-field Correction

Ram Singh
Department of Computer Science and Engineering
Punjabi University, Patiala-147002, Punjab, INDIA
E-mail: bhankharz@gmail.com

ARTICLE INFO: Received: 03 Nov 2024 Revised: 18 Dec 2024 Accepted: 29 Dec 2024

Abstract

Random noise and bias field artifacts in magnetic resonance images (MRI) significantly degrade image quality and destroy essential spatial image information. These factors result in uniform distortions, smoothing variations in low-frequency MR signals, and irregular intensity distributions, severely affecting the original image data across the image regions. The magnetic bias field effects introduce varying intensity variations among tissue regions with similar physical properties that cause dark shading effects, specifically in low-resolution image regions. MR images affected with noise and bias-field or intensity inhomogeneity result in inaccurate interpretation, flawed analysis, incorrect segmentation, and misinformed visual understanding. This paper introduces a deep learning (DL) based feature-aware residue-learning encoder-decoder generator convolutional neural network (RLDCNN) model with a discriminator module to restore quality images from real and fake generated images. The generator model reproduces image information in high-frequency intensity regions using auto-encoding operations. The experimental performance of the proposed method shows minimization of information loss, improved peak-signal-to-noise ratio (PSNR), and structural similarity index measurement (SSIM) values on publicly available brain MRI datasets, BrainWeb, and IXI. The experimental results significantly show improved performance compared to existing MRI denoising methods with 37.83 and 36.35 averaged PSNR, 0.962 and 0.965 averaged SSIM with Brainweb and IXI real MRI dataset with noise levels from 3% to 15% respectively. The averaged bias-field correction result achieved at 34.00 PSNR and 0.974 SSIM in bias corrected images which is significantly higher than the existing methods.

Kay-words: bias-field correction, deep learning, convolution neural network, intensity inhomogeneity removal, magnetic resonance image denoising, residue learning.

1 Introduction

MRI is a preferred noninvasive, painless, and safe medical imaging technique to acquire detailed images of internal human anatomy, physiological structures, and soft tissue organs without ionized radiation waves [1]. MRI provides detailed visual information on internal human anatomical structures and soft tissue regions that help radiologists and physicians in clinical diagnosis and prognosis. It offers images of disease-affected human organs such as the prostate, brain, bones, knee joints, and disease progression abnormalities in a specific body part [2]. A strong magnetic field is applied to excite the desired region of interest to acquire the MRI sequences by receiving radio frequency (RF) waves to generate final images of the respective body organ. MRI scanners use two types of magnets: permanent magnets made of ferromagnetic substances & electromagnets and superconductive magnets. The permanent magnets can produce a field strength of 0.5 T, typically used in diagnostic imaging. Superconductive magnets can carry large amounts of current, enabling high magnetic field strengths and producing magnetic fields up to 18 T that are extremely powerful and uniform [3, 4]. The design parameters of the primary magnetic coils of an MR scanner used to acquire optimal quality images, such as magnetic field strength, magnetic field homogeneity, shimming capabilities, and the linearity of magnetic gradient field imposed on the field of view (FOV) during slice selection and spatial encoding of MR signal [5].

Journal of Information Systems Engineering and Management
2024, 9(4s)
e-ISSN: 2468-4376
https://www.jisem-journal.com/ Research Article

During image acquisition, several uncontrollable factors, such as random noise, motion artifacts, and imperfections in scanner coils cause a grainy appearance in the MR images. Non-uniform intensity distributions across the spatial image regions cause significant image quality degradation, leading to colossal information loss. Inhomogeneous intensity distributions diminish essential image features, resulting in geometrical distortion and affecting image intensity uniformity [6] as shown in Figure 1. Since the bias field effects in the MR images are unknown in advance, and the baseline MR images are usually unavailable, post-acquisition image correction techniques are used to recover acceptable quality images, especially in low SNR brain, cardiac, and prostate MR images. The image quality degradation factors seriously affect the visual image analysis, image interpretation, and other image processing tasks, such as image registration, classification, and segmentation [7].

2 Background

2.1 MRI denoising

Historically, many filtering-based conventional MRI denoising techniques have been presented by various scientists such as Wiener filtering [8], sparsely represented MRI denoising with total variational regularization [9], Gaussian smoothing filter [10], bilateral filters [11] which were found effective in low level single noisy images. The frequency transform methods include multi-scale wavelet transforms for MRI denoising. Yang et al. [12] proposed the Radon wavelets transform that shows effective MRI denoising performance and preserved the critical image details. Similarly, Awate et al. [13] proposed a practical approach based on Bayesian probability for denoising diffusion-weighted MR images that preserve maximum essential image features in the recovered images. Anand and Sahambi et al. [14] presented a wavelet-based bilateral noise filtering method, and Anila et al. [15] proposed a contourlet transform-based MRI denoising technique, which showed significant denoising performance and removing noise induced abnormalities in the multi-resolution MR images. Zhang et al. [16] proposed an improved singular value decomposition (SVD) method for real 3D MR image denoising, which shows better denoising performance than other methods. However, the threshold criterion needs to be uniformly specific and standardized for each type of imaging modality and noise level. Buades et al. [17](2005) proposed a non-local means (NLM) denoising algorithm for gray-scale natural image denoising that shows state-of-the-art denoising performance. Later, several versions of the NLM were extended to MRI denoising, such as MRI denoising using NLM [18], NLM for MRI up-sampling [19], non-local PCA [20], non-local MRI up-sampling, adaptive NLM denoising of MRI with spatially varying noise levels [21], fast NLM [22], radom sampling based NLM [23], adaptive multi-resolution NLM [24], and collaborative NLM [25] that shown state-of-the-art performance in MRI noise removal and preserving maximum structural details in the restored images based on non-local pixels neighborhood similarity in image regions. However, these methods have large computational overheads and are very time-consuming. These methods were effective in smaller datasets with low noise levels but were time-consuming and complex. For high noise levels, the performance of these methods adversely affects the quality of the restored images.

The recent progress in DL-based image analysis methods has shown significant performance in various image-based applications, including image quality enhancement, denoising, reconstruction, classification, and segmentation using post-acquisition image processing techniques [26, 27, 28]. Lehtinen et al. [29] revealed that DL models trained with solely noise-corrupted images can occasionally surpass the performance of a model trained with clean data. The CNN-based deep encoder-decoder models prove effective in many image and computer vision applications such as reconstruction, medical image analysis, semantic segmentation, denoising, deblurring, classification, and image registration [30]. Zhang et al. [31] proposed a DL-based, very effective noise residue learning denoising CNN (DnCNN) method for Gaussian noise removal in MR images. DL methods showed better denoising performance while preserving essential low-frequency features and eliminating strong noise effects. Tripathi et al. [26] proposed a novel local and global residual learning encoder-decoder CNN model (CNN-DMRI) for MRI denoising that achieved excellent results with different MRI datasets. Wu et al. [28] proposed a parallel residual learning CNN model for Rician distributed 3D magnitude MRI denoising (3D-Parallel-RicіaNet) by combining local and global image information. The dilated convolution residual (DCR) module expands the receptive field to avoid global feature loss, and the

Journal of Information Systems Engineering and Management
2024, 9(4s)
e-ISSN: 2468-4376
https://www.jisem-journal.com/ Research Article

depthwise separable convolution residual module preserves the channel and location information. It shows superior denoising and reconstruction performance regarding PSNR, SSIM, and entropy values. Brain et al. [32] proposed a DL residual denoising reconstruction for faster T2-w fluid-attenuated inversion recovery (FLAIR) brain MRI acquisition and proved promising performance with higher signal-to-noise ration (SNR), contrast-to-noise ratio (CNR) and artifact reduction without compromising the image quality. The diffusion models shown effectively enhanced denoising performance in medical image restoration [33, 34, 35] and are now gaining popularity in the medical denoising domain. The iterative DL approach has shown a significantly improved ability to extract pixel-based gradient information in noise-corrupted images without explicitly estimating the prior noise levels in MR images for improved MRI denoising.

2.2 Bias-field distributions

Bias-field effects occurred in MR images with imperfections in scanner coils, and it provides low-contrast quality images with smoothly varying intensity distributions as shown in Figure 1.

Spatial MRI features are badly affected in MR images, especially in images acquired via low magnetic powered MR scanners with low-resolution [36]. This phenomenon happens due to eddy electric current effects, poor radio-frequency (RF) receiving coil uniformity, and patient physical anatomy. The correction of inhomogeneous bias-field can mitigate the issue of low-contrast, over-smoothing, and distortion effects in the acquired images [37]. The main magnet of an MRI scanner generates a static field, denoted as B that is usually homogeneous across the scanning volume but often has inherent imperfections due to the design and environmental factors. B is critical because it polarizes the nuclear spins, aligning them in a uniform direction [3]. A necessary non-parametric bias correction method is N3 [38], which iteratively estimates the multiplicative bias field and actual values of pixel intensity. The non-parametric bias correction method minimizes the entropy of intensity distributions in the pixel brightness by approximation. This method solves several tissue parametric problems in feature extraction but is limited to working with only a single input image. [39] proposed an automated non-parametric MRI inhomogeneity correction method by estimating the bias field from only positive highest pixel values, assuming that the bias-affected images have more information than the original one acquired. High-contrast MRI is desirable for high-precision imaging applications. Various studies for bias correction and intensity normalization techniques for brain and prostate T1-W and T2-W type MRI [40, 41, 42] have recommended the bias correction before intensity normalization to avoid adverse damage to image quality [43]. Xu et al. [44] proposed a methodology to correct noise and bias fields in MR images for segmentation on point-to-point-based algebraic distance constraints. The N4ITK bias correction algorithm requires skull stripped and foreground extracted MRI datasets, which might depend on background removal accuracy, bias field initialization history, and B-spline distance [45]. N4ITK is good at bias-eliminating bias, but its execution is prolonged and time-consuming.

The famous state-of-the-art bias correction method N3, a predecessor of N4ITK, outperforms other existing bias correction methods[38]. N4ITK has also been used for comparison studies of the MRI bias correction [46, 47]. Legar et al. [48] proposed a fully automated physical correction model for detecting intensity distortions in MR images by maximizing the essential image information containing Shannon entropy. Most existing methods focus on simulated MRI with known bias parameters and approximate the target image on a prior reference ground-truth image [47, 49]. Some methods reproduce radiomic image features by evaluating the intensity inhomogeneity correction by suppressing the scanner hardware effects and other artifact removal techniques [50, 51]. An effective adaptive technique for tissue segmentation and bias field reduction in MRI has been reported in [52]. These methods use the optimization of multiple intrinsic components (MICO) for preserving edge and intensity bias correction for measuring inhomogeneity levels in image segmentation applications [53].

3 Problem genesis

During MRI acquisition, the noise in the raw MR signal follows a degenerative model $\mathbf{Y} = \mathbf{I} + n$, where $\mathbf{I}$ noise-free original MR signal and n is the additive white Gaussian noise (AWGN) with standard deviation .
Since image restoration from noise-degraded MR data is an inverse regularization problem, a noise residual

Journal of Information Systems Engineering and Management
2024, 9(4s)
e-ISSN: 2468-4376
https://www.jisem-journal.com/ **Research Article**

learning approach can effectively restore quality images without losing essential information and preserve maximum image information. The noise generation model can be written as:

$$\mathbf{Y} = F(\mathbf{I}) + \mathbf{n} \tag{1}$$

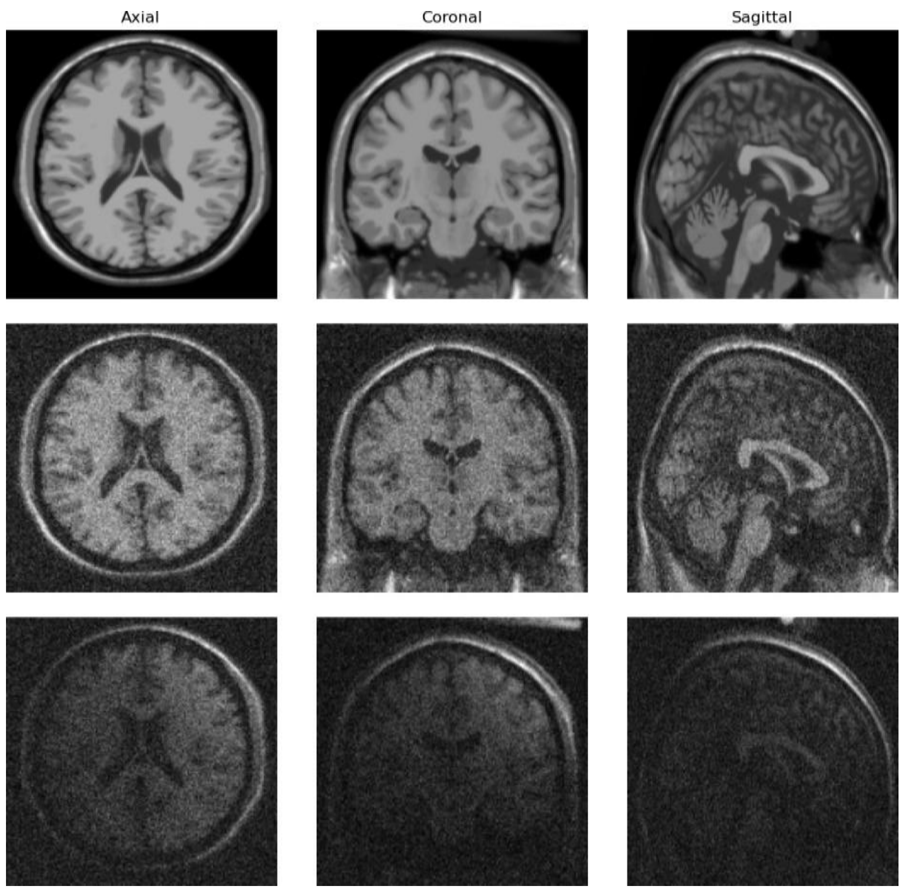

(a) Simulated noise and bias field effects: top row a clean 3D MRI slices of axial, coronal and sagittal views, middle row corresponding noise corrupted images and third row noise and bias affected images

Journal of Information Systems Engineering and Management
2024, 9(4s)
e-ISSN: 2468-4376
https://www.jisem-journal.com/ **Research Article**

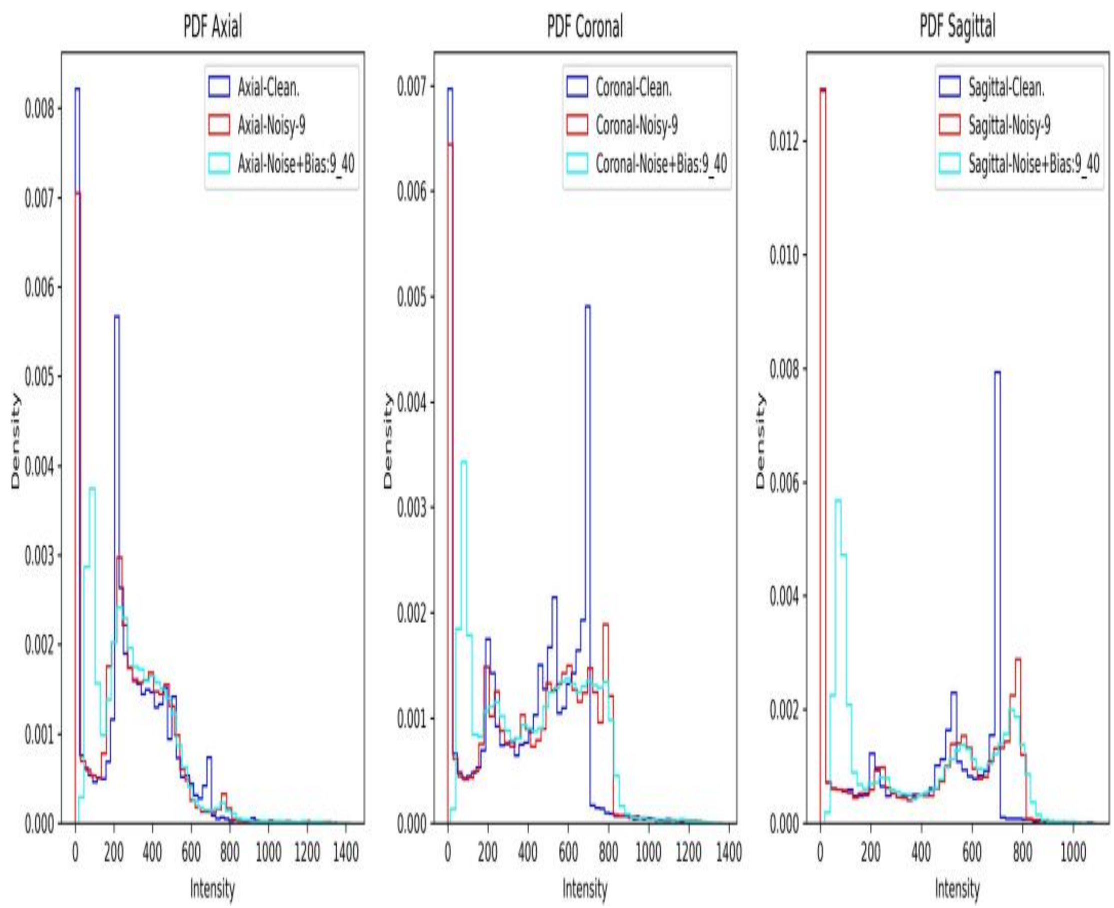

(b) Probability distributions of all above three types of images

Figure 1: Noise and bias field affected 3D MRI slices probability distributions of each

where **I** is original raw k-space MR data acquired in the complex frequency domain, F is the forward Fourier transform operator, **n** is the noise components, and **Y** is the observed noise degraded MR image. The inverse of this forward operation is to recover the approximated **I** from **Y**. However, this problem is typically ill-posed and does not guarantee a unique and stable solution. In addition to noise, an MRI is also affected

Journal of Information Systems Engineering and Management
2024, 9(4s)
e-ISSN: 2468-4376
https://www.jisem-journal.com/ **Research Article**

by the inhomogeneous magnetic field effect, , that causes smoothly varying bias-field effects, also called intensity inhomogeneity, across the spatial image regions. A combined model for noise and bias-field effects can be represented as follows:

$$\mathbf{Y}_{noise\quad bias} = \mathrm{F}(\mathbf{I}\qquad) + \quad(\mathbf{n}) \tag{2}$$

where the function (.) denotes the noise effects with : R^N R^N as random additive Gaussian probability **n** in a 3D voxel of dimensions $N = (x, y, z)$.

The original complex domain MR signal **I** includes both; *real* and *imaginary* part with 90° phase angle difference. Both, signal components got infected with independent random Gaussian noise of zero mean and equal variance. The bias field is typically modeled as a smooth, low-frequency field which can be represented using basis functions as polynomials or splines. The complex domain noise and bias field affected MR signal can be modeled as follows:

$$\mathbf{Y}_{N_{noise+bias}} = \mathbf{I}_N \quad {}_N + \quad(\mathbf{n})_N \tag{3}$$

The visual magnitude MR images reconstructed from calculations of square root of sums of both parts of complex domain via inverse Fourier transforms of coefficients of the degraded MR data. The noise characteristics remain unchanged in the resulting image due to domain orthogonality and linearity properties of the Fourier transform that follows closed correlated associations. Mathematically, the reconstruction of magnitude image **M** from the complex domain MR data is represented as:

$$|\mathbf{M}_N| = \sqrt{(\mathbf{I}_{\Re N} \qquad {}_N + \qquad {}_{\Re N} + \mathbf{I}_{\Im N} \qquad {}_N + \quad {}_{\Im N})} \tag{4}$$

where and indicates *real* and *imaginary* parts respectively in complex domain MR signal. The and parts of noise are assumed to be independent and homogeneously distributed with zero mean and standard deviation .

3.1 Noise and bias field characteristics

The probability distribution of a magnitude MRI generated from the noise-corrupted MR signal obeys Rician probability that contains constant variance across the image regions and follows stationary characteristics [63]. The likelihood of the noise and bias-field affected magnitude MR images is characterized as follows:

$$p(\mathbf{M}_N\,|\,I_N, \quad {}_n) = \frac{|\mathbf{M}_N|}{\quad{}_n} \exp \frac{-(\mathbf{M}^2_{(N)}\quad)+(I^2_{(N)}\quad)}{2\sigma_n^2}\, \mathbf{B}\, \frac{\mathbf{M}_N\, I_N}{\quad{}_n}\, u(\mathbf{M}) \tag{5}$$

where **M** is now corrupted magnitude MRI that follows Rician probability distributions, **I** is the complex domain MR data sequences affected with additive nature Gaussian noise in real and imaginary parts, **B** is 0^{th} order Bessel function of first kind and $u(.)$ is a Heaviside step function.

The nature of the probability of Gaussian noise changed from independent and identical distributed (i.i.d) additive random to signal-dependent correlated, which becomes very difficult to eliminate in MR images.

4 Methods

The primary motive is to recover an acceptable quality denoised MRI $\mathbf{I}'_N$ from the noisy corrupted MR data $\mathbf{Y}$ $\mathrm{R}^{x \times y \times z}$. The expectation $\hat{I}_N = g(\mathbf{Y})$ is the recovered denoised MR image using g; for simplification, the denoising operation to calculate an optimal approximation of g is as follows:

$$\mathbf{I}_N = \underset{\mathbf{g}}{\mathbf{argmin}} \| {}^{-1}\mathrm{F}(\mathbf{Y}) \quad \mathbf{I} \| \;+\; \| \mathrm{L}(\mathbf{I}) \| \tag{6}$$

where the first part of Eq. (6) denote the denoising operation, and the second term L denotes the regularization operator with as a controlling parameter. The approximation of the correct estimation of true MR signal **I** and the bias field parameter is essentially required to recover the maximum image information.

Journal of Information Systems Engineering and Management
2024, 9(4s)
e-ISSN: 2468-4376
https://www.jisem-journal.com/ **Research Article**

A prior-based image features the regularization technique followed in this work, and mathematically, the same is written as follows:

$$argmin = \left\{ \| \mathbf{Y} \quad F(\mathbf{I} \quad) \| \quad + \quad R\ (\mathbf{I}) + \quad R\ (\ ) \right\} \tag{7}$$

where $\| \mathbf{Y} \quad F(\mathbf{I} \quad) \|$ is the data fidelity term, $R\ (\mathbf{I})$ and $R\ (\ )$ are the regularization terms for image details and bias field in the image regions respectively. and are regularization parameters controlling the trade-off between the fidelity and the regularization terms. Adopting a total variational approach, $R\ (\mathbf{I})$ can be set norm L as $\| \quad \mathbf{I} \|$ and R be set norm-2 as $\| \quad \|$ for enforcing smoothness in the inhomogeneous intensity regions.

The task given in Eq. (6) can be accomplished by solved using the alternating direction method of multipliers (ADMM) algorithm by reformulating as a constrained problem [64, 65] as follows:

$$\underset{\mathbf{I},\mathbf{v}}{argmin} \| F(\mathbf{I}) \quad \mathbf{I} \| \ + L, \quad s.t. \quad \mathbf{I} = \mathbf{v} \tag{8}$$

The above Eq. (8) can be written as augmented Lagrangian function as follows:

$$L(\mathbf{I}, \mathbf{v}, \mathbf{u}) = \| F(\mathbf{I}) \quad \mathbf{Y} \| \ + L(\mathbf{v}) + \mathbf{u}^T (\mathbf{I} \quad \mathbf{v}) + \frac{}{2} \| \mathbf{I} \quad \mathbf{v} \| \tag{9}$$

where $\mathbf{u}$ and are Lagrange multipliers. Eq. (7) can be used by minimizing it to solve other sub-tasks by getting saddle point of L as:

$$\mathbf{v}^k \quad = \underset{\mathbf{v}}{argmin}\ L(\mathbf{v}) + \frac{}{2} \| (\mathbf{I}^k + \mathbf{u}^k) \quad \mathbf{v} \| \tag{10}$$

and;

$$\mathbf{I}^k \quad = \underset{x}{argmin} \| F(x) \quad \mathbf{Y} \| \ + \frac{}{2} \| \mathbf{I}^k \quad (\mathbf{v}^k \quad \mathbf{u}^k) \| \tag{11}$$

and $\mathbf{u}^k$ is obtained from $\mathbf{u}^k + (\mathbf{I}^k \quad \mathbf{v}^k \quad)$.

A sub-task given in the Eq. (10) can be treated as a denoising task [66] by re-writing it as follows:

$$\mathbf{v}^k \quad = \underset{\mathbf{v}}{argmin}\ L(\mathbf{v}) + \frac{1}{} \| \mathbf{v} \quad \tilde{\mathbf{v}}_{\mathbf{k}} \| \tag{12}$$

where $\tilde{\mathbf{v}}^{\mathbf{k}} = (\mathbf{I}^k + \mathbf{u}^k)$ that representing the Gaussian noise corrupted image with standard deviation, which is measured it at each k^{th} iterations. A denoising model $\mathbf{f}_L$ can be trained to denoise the given input images as:

$$\mathbf{v}^k \quad = \mathbf{f}_D(\mathbf{v}_{\mathbf{k}}, \ ^k) = \mathbf{f}_D(\mathbf{I}^k + \mathbf{u}^k, \ ^k) \tag{13}$$

where $\mathbf{u}^k$ is used to estimate the residual component that updates from $\mathbf{u}^k + (\mathbf{I}^k \quad \mathbf{v}^k \quad)$. The bias-field correction can be solved by preserving maximum essential local and global features by attention-guided discriminative network by following formulation:

$$\mathbf{x}^k \quad = \mathbf{G}(\mathbf{Y}^k) = \mathbf{G}(\mathbf{v}^k \quad \mathbf{u}^k) \tag{14}$$

where $\mathbf{G}$ is the generator model and $\mathbf{Y}^k = \mathbf{G}(\mathbf{v}^k \quad \mathbf{u}^k)$ is the k th bias-affected MR image.

The information loss in the recovered images $\mathbf{I}_{clear}$ and the input noisy image by learning and preserving maximum essential image features using learnable training parameters . The information loss is calculated by measuring the averaged mean squared error (AMSE) between both images as:

$$L(\ ) = \frac{1}{N} \sum_{x,y,z}^{N} \| F(M_{x,y,z} \ ; \ ) \quad M_{x,y,z} \| \tag{15}$$

where N is the size of training datasets.

4.1 Bias field modeling

Let an MRI volume sequence m contain n number of voxel per volume, and $X = [X , X , X , ..., X_n]$ $\mathbb{R}^{m \times n}$ be the transmitted log-intensity tensor that is corrupted with some additive log-bias intensity $\mathbb{R}^n$. Additionally, let Z_i $[K]$ be the tissue region for i^{th} voxel. The multi-sequence log-intensity for a vector X_i will be conditionally characterized by a multivariate normal given below:

$$X_i | (Z_i = k, \quad _i) \quad \Upsilon (\mu_k + \quad _i \mathrm{d}_m, \quad _k) \tag{16}$$

where d_m is the m-dimensional vector of ones, μ_k $\mathbb{R}^m$ and $_k$ $\mathbb{R}^{m^2}$ are unknown Gaussian parameters. The probability of bias field appears to vary slowly in image space with the Gaussian prior:

$$\mathrm{N}\left(0, \quad L^{\dagger}\right) \tag{17}$$

where $L^{\dagger}$ represents the pseudo-inverse graph Laplacian along with the spatial structure of scanning parameter $^{-}$ as a log-bias gradient penalty regularization parameters. The expectation maximization for a posterior probability is considered in the dark image regions with:

$$\arg\max p \quad (X, B) \tag{18}$$

where parameters and B are selected conditionally independent of each other, with an assumption of improper uniform prior p $= 1$. *argmax* is an invariant and monotonic scaling transformer for generating an equivalent long probability of the joint probability defined as:

$$\arg\max \log p \quad (X, B) \tag{19}$$

where probability normalization parameter p (X) must decrease. A function $f(\quad)$ is to be called minorized by $g(\quad | \quad ^t)$ when $=$ ^{t} if:

$$g(\quad | \quad t)) \quad f(\quad), \text{for every} \tag{20}$$

Our goal for $X = \{X_i\}^n_i$ is to show that:

$$\begin{aligned} g(\quad B | \quad ^t, B^t) &= Q(\quad B | \quad ^t, B^t) \\ &+ \log p_{\ (t)}(X, B^t) \\ &Q\left(\quad ^t, B^t | \quad ^t, B^t\right) \end{aligned} \tag{21}$$

is a minorizing system of $(\quad B)$ is mapping into the $\log p\ (X, B)$ at $\left(\quad ^t, B^t\right)$, where:

$$Q(\quad | \quad ^t, B^t) = \mathrm{E}_{\theta p_{(t)}(Z|X, B^{(t)})} [\log p \quad (Z, X, B)] \tag{22}$$

An auxiliary distribution $q(Z)$ can be achieved by decomposing the KL divergence of q and probability p with the following:

$$D(q \| p \quad) := \mathrm{E}_{Z \sim q}\left[\log \frac{q(Z)}{p}(Z | X, B)\right] \tag{23}$$

The minorization-maximization can iteratively applied for the expectation-maximization (EM) by:

$$Q(\quad B | \quad ^t, B^t) = \mathrm{E}_{p_{\theta(t)}(Z|X, B^{(t)})} [\log p \quad (B, X, Z)] \tag{24}$$

with

$$(\quad ^t \quad, B^t \quad) = \arg\max Q(\quad B | \quad ^t, B^t) \tag{25}$$

The above parameters (^{t} and B^t) cannot be optimized because they are not independent of each other. The bias estimation process of the EM is separated from Gaussian probability and bias intensity estimates to provide updates of couple-closed expectations and written as:

Journal of Information Systems Engineering and Management
2024, 9(4s)
e-ISSN: 2468-4376

https://www.jisem-journal.com/ **Research Article**

- Expectation update:

$$w_{ik} = \frac{p(X_i | Z_i = k, B)}{\sum_l^K p(X_i | Z_i = l, B)} \tag{26}$$

- Gaussian update:

$$_k = \frac{1}{n}\sum_i^n w_{ki} \tag{27}$$

$$\mu_k = \frac{\sum_i^n w_i k (X_i \quad B_i 1m)}{\sum_i^n w_i k} \tag{28}$$

and

$$_k = \frac{\sum_i^n w_i k (X_i \quad \mu_k \quad B, 1m) \times (X_i \quad \mu_k \quad B, 1m)^T}{\sum_i^n w_i k} \tag{29}$$

- Bias field update:

$$B = \left(\frac{1}{} + \sum_k^K 1_m^T \sum_k 1_m diag(w.k)\right)^{-} \times \left(\sum_k diag(w.k)(X \quad \mu_k 1_n)^T \sum_k 1_m\right) \tag{30}$$

Here, (.) is the subsequent iterative parameters estimation for the given current parameter (.) that update with random permutation convergence. These updates are optimized using first-order decision variables to increase the search for parameters for concave targets for increased parameter exploration [67, 68].

$$\arg\max p\,(B | \{X_i\}_i^n) \tag{31}$$

The final objective of the network is to learn the essential image features from the training data by minimizing a combined loss for both noise and bias field estimation to preserve the image quality by data loss minimization function L as follows:

$$\mathrm{L} = \|\mathbf{Y} \quad \mathrm{F}(\hat{\mathbf{I}} \quad \hat{}\,)\| + \mathrm{R}\,(\hat{\mathbf{I}}) + \mathrm{R}\,(\hat{}\,) \tag{32}$$

second part deals with minimizing the bias field correction to regenerate artifacts-free MR images.

4.2 Network Architecture

For the denoising task, we used a dilated residual learning model, named RLDCNN, that extracts and preserves local & global spatial features. RLDCNN contains dilated convolution (deConv), residual learning, batch-normalization, and Leaky Rectified Linear Activation Unit (LReLU). We obtained the residual noisy images by subtracting approximated noisy sub-images from each intermediate generated image with convolution operation to improve the network ability by updating the feature learning process. The BN layer generalizes the network improvement ability. LReLU activation function controls the gradient vanishing points and Gaussian smoothness. A zero-padding was added to image boundaries during dilated convolution to make the output the same as the input. The first two levels of the network have 96 feature channels, with 48 channels in each level for dilation 1 to 3 during convolution filtering. At the third level, 32 feature channels concatenate all feature channel outputs. The dilated convolutions preserve the global image features and ignore the local fine details. To extract and preserve the local feature information, we integrate two

Journal of Information Systems Engineering and Management
2024, 9(4s)
e-ISSN: 2468-4376
https://www.jisem-journal.com/ **Research Article**

depthwise separable convolution operations with the BN layer after other convolution operations to control the vanishing gradients and network generalization performance. RLDCNN contains 18 convolution residual modules with different dilation rates r. The filtering dimensions are set to 3×3 and $3 \times 3 \times 3$ for 2D MRI slices and 3D MRI voxel, respectively. To suppress the gridding effect that appears due to dilated kernels in the higher convolution layers, different r values are used for other modules ranging from 1 to 3 and in the final reconstruction module set as 1. The lower value of r also controls the gridding effects. The overall architecture of the denoising encoder-decoder modules is illustrated in Figure 2.

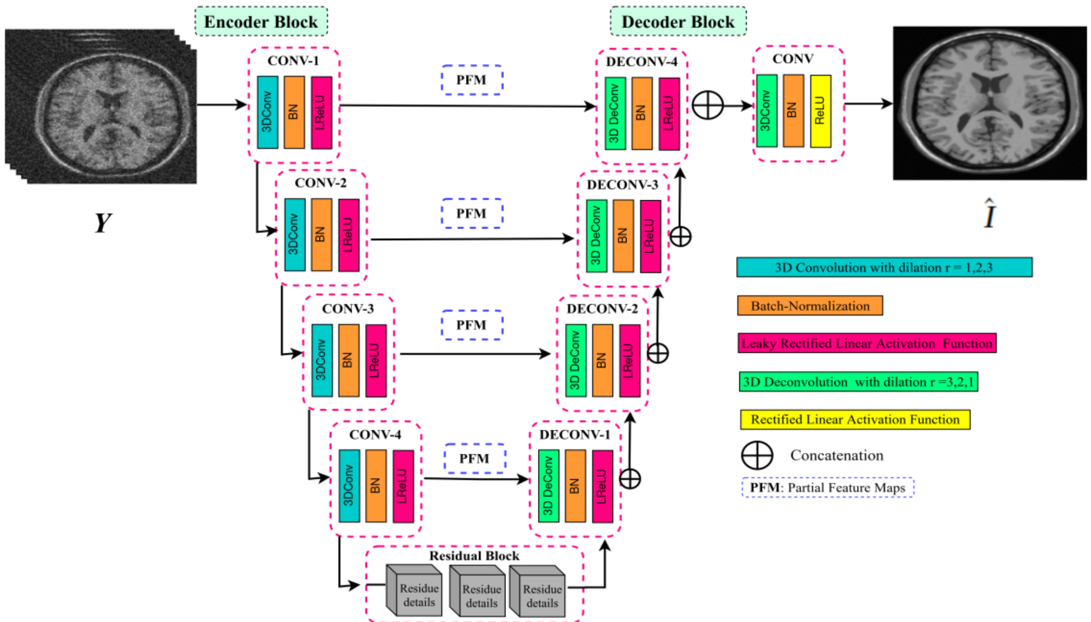

Figure 2: Dilated residue learning MRI denoising encoder-decoder network architecture

Each sub-module of the network contains 16 convolution-filtering kernels. The output features from each module fused gradually to realize the restoration of local and global information in the denoised images. Finally, the reconstruction layer enables the estimation of the information loss in the denoised images by calculating the deviation $g = (\mathbf{Y};$

image by $\hat{\mathbf{I}} = \mathbf{I}$ $g(\mathbf{Y};$

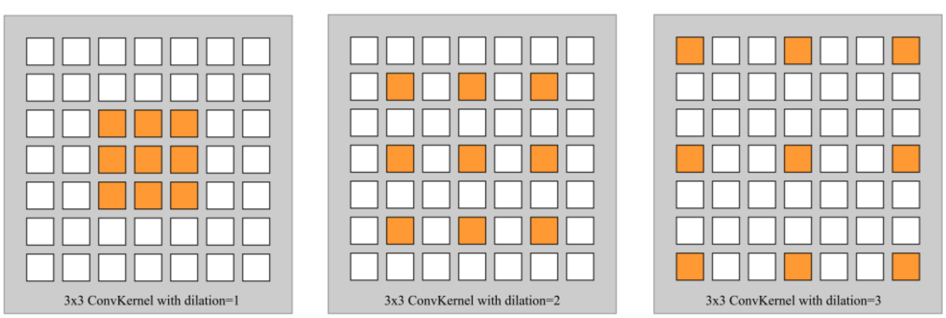

Figure 3: Convolution filtering kernels with different dilation rate

The convolution filtering kernels have dilation rates of 1 and 2 levels. To prioritize maximum feature preservation and minimize information loss in the denoised images, we opted for convolution filters with a dilation rate of 1. The choice of dilation rate depends on the receptive field sizes. Figure 3 show dilated filtering kernels with different dilation rates (r) are demonstrated to capture various receptive fields

$$r = ((k_{size}) \quad 1) \times (r \quad 1) + k_{size})^d \tag{33}$$

Journal of Information Systems Engineering and Management
2024, 9(4s)
e-ISSN: 2468-4376
https://www.jisem-journal.com/ **Research Article**

where k_{size} is the kernel size, r is the dilation rate and d is width of the image. The increase in dilation rate leads to expanded receptive fields. However, it leads to the loss of critical spatial image features. The increased r creates a tradeoff with a wider receptive field, which leads to essential feature loss in the MR images. To avoid these drawbacks, many authors have proved the effectiveness and advantages of dilated convolutions for quality image restorations [69, 70]. The first denoised MR image contains partial feature maps (PFM) of the input data, and the model relearns **P** features to update the weight parameters by adding it back to PFM. The new information details are reacquired by a detail preserving and relearning process $\mathbf{P}'$, objectively minimizing the difference between the **P** and $\mathbf{P}'$ by calculating the mean squared error between the input and target image. It is defined here as follows:

$$= \frac{1}{2N} \sum_{i}^{N} \|\mathbf{P}'(\mathbf{y}_i ; \quad \mathbf{P}(\mathbf{y}_i ; \| \tag{34}$$

where $\mathbf{y_i}$ denotes a noisy *ith* sub- N is the number of input noisy images during the training phase. The residual image $\mathbf{r_i}(\mathbf{y_i};\ )$ learn the noise details during the noise $\mathbf{n_i}$ removal to obtain noise-free denoised image **P** by the following process:

$$\mathbf{P}(\mathbf{y_i}; \quad = \mathbf{r}(\mathbf{y_i}; \quad \mathbf{n_i} \tag{35}$$

In the residue learning, the noise part $\mathbf{n_i}'$ tends to be very close to $\mathbf{n_i}$. According to generative noise model, noise part $\mathbf{n_i}$ is approximated to:

$$\mathbf{n_i} = \mathbf{y}_i \quad \mathbf{X}_i \tag{36}$$

where $\mathbf{y_i}$ is a noise corrupted image and $\mathbf{x_i}$ is a noise free image. Therefore, according to Eq. (35) and Eq. (36), the denoised image can be represented as:

$$\mathbf{P}(\mathbf{y}_i; \quad \mathbf{r}(\mathbf{y}_i; \quad \mathbf{n}_i = \mathbf{r}(\mathbf{y}_i; \quad (\mathbf{y}_i \quad \mathbf{x}_i) \tag{37}$$

In order to address issues such as over-fitting, loss of critical contextual information, and reduce the number of network parameters, we decided to use a smaller receptive field. Although larger receptive fields capture more global contextual information, they also lead to an increase in parameters and can result in over-fitting, as described by Yu et al. (2015). Additionally, increasing network depth can lead to vanishing gradient problems. The loss estimation function given in Eq. (K0) can be transformed as follows:

$$= \frac{1}{2N} \sum_{i}^{N} \|\mathbf{P}'(\mathbf{y}_i ; \quad \mathbf{r}(\mathbf{y}_i ; \ + (\mathbf{y}_i \ \mathbf{x}_i)\|_i \tag{38}$$

$$= \frac{1}{2N} \sum_{i}^{N} \|[\mathbf{y}_i \quad \mathbf{r}(\mathbf{y}_i ; \quad + \mathbf{P}'(\mathbf{y}_i ; \quad \mathbf{x}_i)\|$$

In this approach, the PFM $(\mathbf{y}_i \quad \mathbf{r}(\mathbf{y}_i;$ is computed by subtracting the residual $\mathbf{r}(\mathbf{y}_i;$ from the noisy image $\mathbf{y}_i$. The denoising process incorporates information from the residual features to ensure preservation of essential image details. Utilizing multi-level dilated convolutions from the second to seventh layer enhances the extraction of spatial features for updating the PFM. These convolutions also optimize space for subsequent network operations, facilitating the learning of additional features to effectively remove noise from MR images.

4.3 Bias correction model

In order to correct the bias-affected MRI images while preserving unbiased pixel intensities and local tissue regions, the proposed model needs to accurately estimate the pixel intensity values in the affected images. The application of multi-scale bias removal filters aids in deriving the true pixel intensity values. The architecture of the bias-field correction network is illustrated in Figure 4. To capture more parameters, larger filtering kernels with a wide receptive field are used, but they introduce computational complexity. By employing dilated kernels with a skip-connections strategy, the need for multiple function applications can be significantly reduced to avoid macro views [60]. While dilated convolutions require fewer parameters and help in preserving local neighborhood information, excessive dilation can lead to gridding effects and inconsistent semantic clustering of pixel values [72]. The use of zero padding between filtering kernels does not store image information but produces the same output as the input images. Horizontal and vertical convolution operations mitigate the bias effect of dilated convolutions. Additionally, the deformation operation extracts macroscopic contextual information, and the 2D/3D filter core provides local contextual and neighboring information.

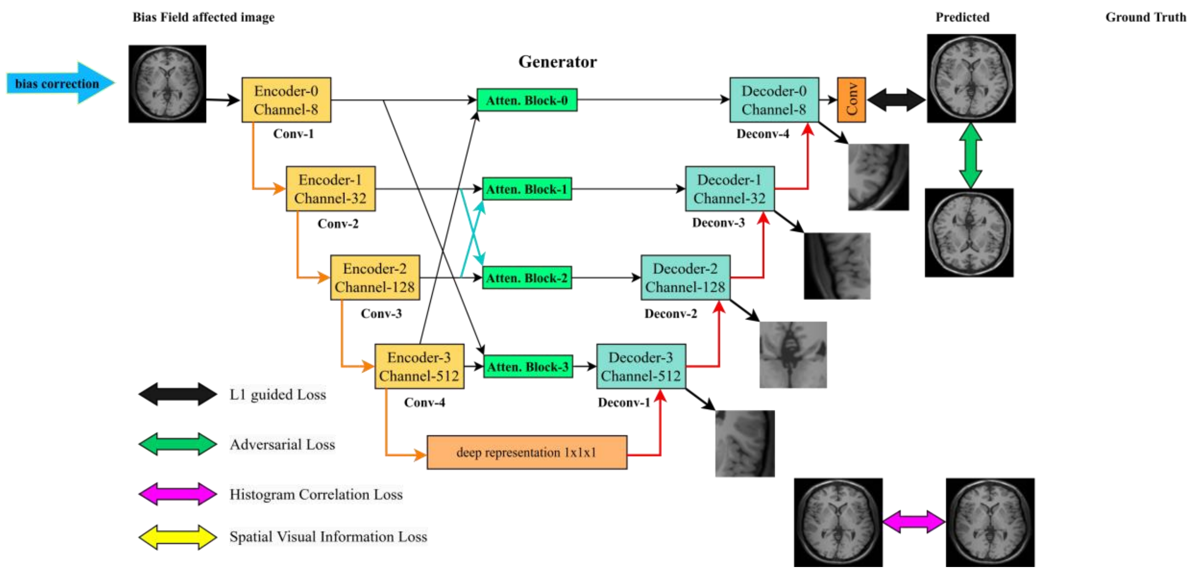

Figure 4: Attention-driven skip-connection encoder-decoder generator network for bias-field correction

Figure 5 depicts the design of a proposed bias correction model composed of four 3×3 kernels with different receptive fields and dilation connection expansions of 1, 2, 4, and 6 points along with the horizontal and vertical skip-connection convolutions.

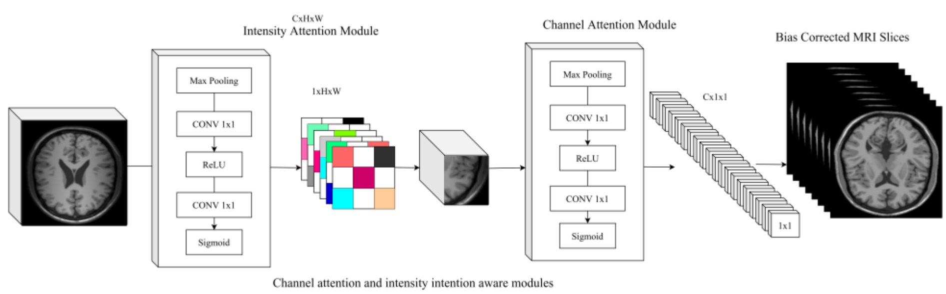

Figure 5: Attention-driven skip-connection encoder-decoder generator network for bias-field correction

The convolution operation involves applying square-sized dilated filtering kernels with dimensions of 3x3, 5x5, 9x9, and 13x13 on both the horizontal and vertical axes to expand different receptor fields. Additionally, corresponding horizontal and vertical kernels of dimensions 1x3, 1x5, 1x9, 1x13, 3x1, 5x1, 9x1, and 13x1 are used respectively.
is combined by channel concatenation. The feature maps extracted from dilated outputs are compared to each convolution kernel output by taking the average of the output values to obtain maximum feature information. The results of the dilated kernels are resized to 1x1, maintaining the output depth at the channel
M The network weight parameters are iteratively updated by incorporating residual learning to update the channel weight and extract more detailed properties during convolution operations by mapping and removing ground truth images.

Journal of Information Systems Engineering and Management
2024, 9(4s)
e-ISSN: 2468-4376
https://www.jisem-journal.com/ **Research Article**

4.4 Feature aware dilation

The automatic encoder block in the down-sampling network increases the inputs to the contextual semantics and spatial information locations in the image region. The skip-connection and dilated convolution between the encoder-decoder blocks optimize the spatial intensity levels and contextual information in all the data blocks. The attention-driven dilated encoder network transfers optimal contextual and spatial image information from the encoders to the decoders. These dilated connections reduce the intensity of non-uniformity by correcting spatially localized image pixels based on specific region semantics. The spatial attention-network channels select the desired feature map of sizes $c \times h \times w$ and generate the feature map of $c \times 1 \times 1$ and $1 \times h \times w$. The channel and spatial attention blocks acquire the essential feature blocks from the improved feature maps. Therefore, attention blocks provide new updates to scale the main feature maps, focusing on less informative features. The essential feature maps were extracted by combining the scaled feature maps with channels and spatial attention blocks, as shown in the Figure 5.

4.5 Generator module

The generator network comprises four encoder-decoder blocks and one final fully connected output layer. Each block consists of a multi-scale local information module. The model proceeds with downsampling the essential features by a factor of 2 through a reverse pixel shuffling operation [73, 74, 75]. The encoding blocks encode the vital characteristics and represent them at a deep convolution level. On the other hand, the decoder blocks input characteristic maps via pixel shuffling methods and concatenates them with the main feature maps of the attention blocks. The decoder blocks generate two outputs: one to the next decoder block and the other to predict a clean, uniformly corrected output image. After the pixel shuffling via convolution operations, output image dimensions are mapped to the ground truth reference image. The final prediction from the bias field affected was obtained using 3×3 convolution kernels. The discriminator block predicts the bias-free intensity level, distinguishing between the reference pixels and false results compared to the ground-truth images. The discriminator manipulates the overlapped image patches to classify them as non-biased or biased image patches. The discrimination blocks are implemented in the same way as proposed in [60].

4.6 Loss Estimation

The overall complete information loss estimation function is defined as follows:

$$\mathrm{L} = \mathrm{L}_L \; + \quad \times \mathrm{L}_{ADV} + \quad \times \mathrm{L}_{HistCorr} + \quad \times \mathrm{L}_{\;D} \tag{39}$$

where the terms , and values are set to 10, 1, and 100 after the number and are used to add weight parameters to control the network performance.

The L1 regularizer has been used to minimize the aggregate errors obtained from the differences between values of the ground truth images and the predicted images sum of all absolute differences. The up-sampling process is improved by comparing the predictions from each encoder-decoder block with the L1 data loss L to the ground-truth reference image, and the same is written here as:

$$\mathrm{L}_L = \sum_i^D \sum_j^n \left\| (f^G_{i,j} \quad f^P_{i,j}) \right\| \tag{40}$$

where L and n represent the decoding levels and the number of image patches, respectively, where $f^G_{i,j}$ and $f^P_{i,j}$ are ground truth and predicted image patches respectively.

4.6.1 Adversarial Loss

The generator network model provides field-corrected bias MR images with a clean bias, bias-free ground truth image. The generator model G captures the data distribution, and the discriminator D estimates the probability pD in the input data. When the generator divides p over input data f, it maps from the previous noisy distribution $p_z(z)$ to a single vector space image that is called G(z; $_g$).

Journal of Information Systems Engineering and Management
2024, 9(4s)
e-ISSN: 2468-4376
https://www.jisem-journal.com/ **Research Article**

The discriminator, $D(f;\ _d)$, generates a single scale probability distribution of data from training data that is not p_g but f. Here, the generator blocks G to minimize the discrimination to classify output predictions from reference samples, while the discriminator D tries to maximize its ability to classify the maximum prediction close to the ground truth references. Information loss is estimated during image reconstruction using an adversarial loss estimation function written as follows:

$$\min \max L_{ADV}(G, D) = E_{f\sim p_{data}\ f}[\log D(f)] + E_{f\sim p_z\ z}[\log(1 \quad D(G(f)))] \tag{41}$$

4.6.2 Histogram-based correlation loss

The pixel-wise intensity histogram shows the distribution of pixel values at each location in an image. An unbiased image shows distinct intensity values for different regions, while biased images show artificially altered intensity values. The histogram visually represents the variations in the frequency distribution of intensity levels. The disparity between these values is utilized to enhance the similarity between the histograms of the ground truth and bias-free images generated by a model. This correlation is used to quantify information loss as described in [60]:

$$D_{Hist}(H_g, H_r) = \frac{\sum_I (H_g(I) \quad \bar{H}_g)(H_r(I) \quad \bar{H}_r)}{\sqrt{\sum_I (H_g(I) \quad \bar{H}_g) \ (H_r(I) \quad \bar{H}_r)}} \tag{42}$$

$$L_{HistCorr} = (1 \quad D(H_g, H_r))$$

where D is the histogram pixel values difference between the ground truth H_g and reference H_r images I, and $L_{HistCorr}$ is histogram correlation between the pixel intensity values of predicted and reference image pair.

4.6.3 3D Spatial information loss

2D slices of MR or 2D segmented images can visualize 3D gray-level MR intensity images. The pixel coordinate position represents the gray-scale pixel values in a 2D image grid on (x, y) or (x, y, z) axis of a $Height(H) \times Width(W) \times Depth(D)$ dimensions. Consequently, the pixel coordinates (x, y) in gray-scale 2D images are between 0 and 255. Similarly, in a 3D image space, the pixel intensity values of a coordinate (x, y, p_i) are 1 and 0. The ground-truth reference and predicted outputs are represented in a 3D MR voxel. The difference between these vectors is calculated by reducing the mean absolute difference and is treated as 3D spatial loss as follows:

$$L_{V_{3D}} = \frac{1}{HWD} \sum_x^H \sum_y^W \sum_z^D \| V^g_{x,y,z} \quad V^p_{x,y,z} \| \tag{43}$$

where $V^g_{x,y,z}$ and $V^p_{x,y,z}$ are 3D MR voxel of the ground-truth reference and predicted outputs, respectively. The overall data loss in all MRI voxel is measured by adding all the loss terms defined above with the following objective function:

$$L = L_{L_{ADV}} + \quad L_L \quad + \quad L_{V_{3D}} + \tag{44}$$

5 Implementation

The Least-Square Generative Adversarial Networks (LSGANs) [76] utilize the least-square error loss for both the generator and discriminator blocks. Regular adversarial generator network models are typically employed to generate new samples from the latent probability distribution p_z. These generated data samples augment training datasets for discriminative models and facilitate data synthesis for expert human analysis. However, synthetic image samples are susceptible to specific errors that can significantly impact medical

rnal of Information Systems Engineering and Management
9(4s)
: 2468-4376
https://www.jisem-journal.com/ Research Article

image reconstruction and analysis. The discriminator model is trained to distinguish between real and fake image pixels generated by the generative network. The loss log-likelihood of the discriminator is calculated

i.e., maximizing the log of $D(x)$, where $D(x)$ represents the classification of an authentic image x. On the other hand, discriminators aim to maximize the probability of correctly identifying false images as fake, transforming a generated image to a (1 $D)(G(z))$ representation that maximizes the log of (1 $D)(G(z))$, where z is a random noise vector or a biased corrupted input image that has been distorted. With a batch size of one, we first applied the Adam optimization function with a learning rate of 0.0001 for the first 50 epochs, and then increased the learning rate linearly from 0 to 100 epochs. The values were determined through a series of operations, with = 10, = 1, and = 100. The proposed methodology employed peak signal-to-noise ratio and structured similarity index metrics for evaluation and performance comparison with other existing methods.

6 Experimental Setup

The bias estimation and correction model created using TensorFlow and evaluated on a 12GB NVIDIA RTX 3080Ti GPU and an AMD Radeon processor with 32GB of RAM. We compared the results by training a U-Net type model on simulated and real MRI datasets with pre-added and added noise variance and bias field effects. The performance was compared with prior ground truth noise and bias-free images as testing and validation sets. We used a batch size of 1 and a learning rate of 0.0001 for the first cycle, with the algorithm linearly decomposing for up to 100 epochs. The experimental testing results were assessed using standard quality metrics PSNR and SSIM values, and cross-validation statistics for K=10 were obtained. We used the TensorFlow framework to construct a U-Net type model and train it with three different MRI datasets to We extracted multi-scale features using convolution kernels with different receptor sizes.
measured by combining the model-generated image histograms with ground truth images through dilated convolution operations along the horizontal and vertical orientations at all scale information. The final results demonstrated better denoising and bias correction performance in terms of PSNR and SSIM values than using only single convolution or dilated-convolution operations. Figure 6 show (a) the training vs validation loss evaluation and (b) show training vs accuracy validation evaluations performance observed in the 100 epochs.

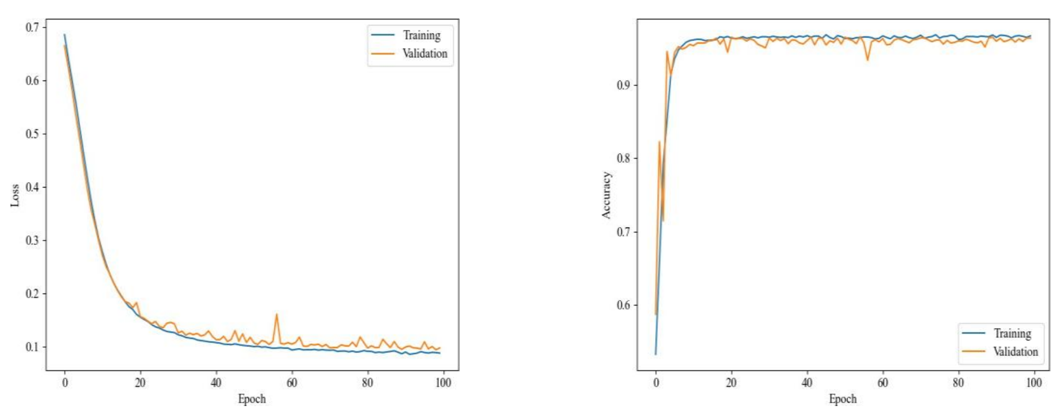

(a) Training vs Validation loss evaluation (b) Training vs Accuracy validation evaluation

Figure 6: Training and Accuracy validation loss evaluation under 100 epochs

Journal of Information Systems Engineering and Management
2024, 9(4s)
e-ISSN: 2468-4376
https://www.jisem-journal.com/ Research Article

6.1 Datasets

The denoising model trained with two datasets from the publicly available open-source MRI datasets Brainweb (https://brainweb.bin.mni.mcgill.ca/brainweb/) and IXI-Hammersmith dataset (http://brain-development.org/ixidataset/). Brainweb is a simulated realistic brain MRI 3D volumes. It is noise-free and affected by varying noise levels in T1-weighted, T2-Weghted, and proton density modality formats. We have considered its T1-weighted for training and testing purposes. The second subset is a real brain MRI dataset IXI [77] containing t1-w MRI scans of 581 subjects. A summary of these both sub-dataset is given in Table 1. We considered noise-contaminated MR images with noise levels 3% to 15% with step 2% to both datasets for denoising evaluation purposes.

Table 1: MRI datasets description used in denoising and bias-field correction tasks

Dataset	Dimensions	Noise Levels	Bias-field	No. of Slices
Brainweb (T1-w)	181x217x181	3 to 15%	20%, 40%	181
IXI (T1-w)	256x256x150	3 to 15%	10% - 50%	150

The original dimensions of the both dataset were down-sampled by reducing their original size to 192×192 and 192 × 192 in the preprocessing stage. In addition, this method has also been tested on an open source IXI brain MR dataset [77] with dimensions 256 × 256 × 150.

7 Image quality measures

Two widely used quantitative evaluation criteria are employed to measure the quality of a restored image. The first metric is peak signal-to-noise ratio (PSNR), and the second is structural similarity index (SSIM). PSNR measures the difference between the restored image and the reference image and is defined as:

$$PSNR(\mathbf{I}, \hat{\mathbf{I}}) = 10 \log \sum \frac{\mathbf{I}_{MAX}}{\sum_{x,y,z \in \Omega} |\mathbf{I}_i - \hat{\mathbf{I}}_i|} (dB) \tag{45}$$

where $\mathbf{I}_i$ and $\hat{\mathbf{I}}_i$ are the image intensities at i^{th} position of original MR images pixels and the restored images, respectively.

Second, SSIM measures the structural similarity considering changes in structural information, luminance, and contrast between the approximated restored image and the ground-truth image. The higher SSIM value closer to 1 implies the better denoising performance and it is written a follows:

$$SSIM(\mathbf{I}, \hat{\mathbf{I}}) = \frac{(2\mu_{\mathbf{I}}\mu_{\hat{\mathbf{I}}} + C_1)(2\sigma_{\mathbf{I}\hat{\mathbf{I}}} + C_2)}{(\mu_{\mathbf{I}}^2 + \mu_{\hat{\mathbf{I}}}^2 + C_1)(\sigma_{\mathbf{I}}^2 + \sigma_{\hat{\mathbf{I}}}^2 + C_2)} \tag{46}$$

where $\mu_{\mathbf{I}}$ and $\mu_{\hat{\mathbf{I}}}$ are the local means, $\sigma_{\mathbf{I}}$ and $\sigma_{\hat{\mathbf{I}}}$ are standard deviations, $\sigma_{\mathbf{I}\hat{\mathbf{I}}}$ is the covariance, and C_1 and C_2 are two constant values to control the intensity instability respectively in both images.

7.1 Denoising results

The experimental denoising performance evaluated using simulated BrainWeb T1-w brain MRI and IXI, a real brain MRI dataset. The BrainWeb is available in noise free and pre-affected with noise levels 3% to 15% in each axial, coronal, and sagittal orientation planes of nifti formats. The observed denoising results obtained in terms of PSNR and SSIM values. The numerical results show better performance of the proposed models than similar other denoising methods. The IXI dataset also corrupted by adding simulated noise levels from 3% up to 15% with increment level 2%. The denoising results obtained from both datasets are shown in tables 2, 3, 4, and 5. Figure 7 shows from (a) to (c) the randomly selected MRI slices from both the denoised datasets, which shows enhanced visual quality while preserving structural details across the image regions.

Journal of Information Systems Engineering and Management
2024, 9(4s)
e-ISSN: 2468-4376
https://www.jisem-journal.com/ Research Article

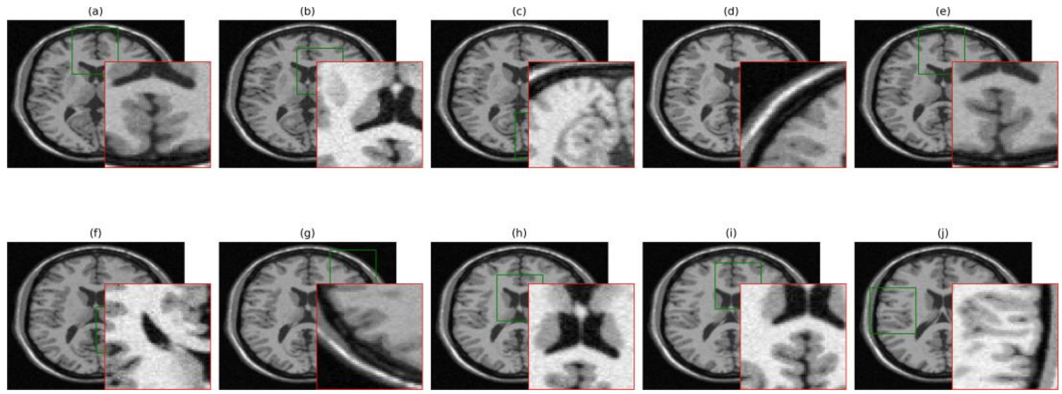

(a) Randomly selected simulated Brainweb noise-degraded MRI with varying noise levels

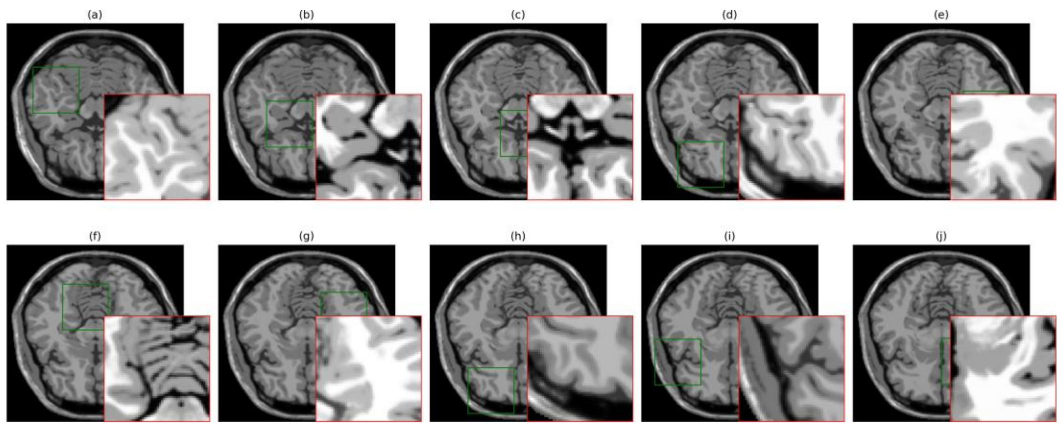

(b) Randomly selected denoised simulated Brainweb MRI results

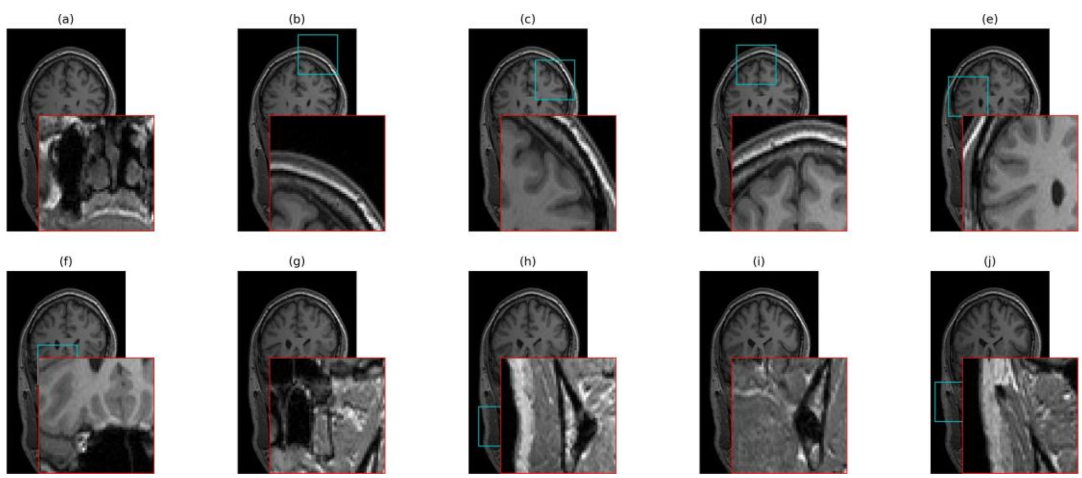

(c) IXI real MRI denoising results

Figure 7: Randomly simulated denoised Brainweb and IXI brain MRI brain dataset MRI corrupted with noise levels from 3% to 15% denoising visual performance analysis

Table 2 and 3 show quantitative results in PSNR and SSIM values of experimental observations. The observed denoising results are also compared with other existing DL-based MRI denoising methods and reveal improved denoising performance with the applied noise levels in MR images.

Table 3 shows SSIM metric values of the proposed method and comparison with other existing methods.

2024, 9(4s)
e-ISSN: 2468-4376
https://www.jisem-journal.com/ **Research Article**

Table 2: Brainweb T1-w MRI denoising performance measure in PSNR values with noise levels from 3% to 15%

Method	**Noise Levels**						
	3%	**5%**	**7%**	**9%**	**11%**	**13%**	**15%**
BM3D	33.19	31.01	30.49	28.91	26.87	25.21	23.39
CNLM	37.18	33.88	33.01	31.58	31.16	30.71	30.13
PRI-NLM3D	38.50	35.67	33.74	32.37	31.14	30.16	29.24
CNN3D	38.46	35.86	33.61	32.79	31.49	29.91	28.69
MCDnCNNg	39.38	37.12	35.40	33.86	32.54	31.10	29.96
MCDnCNNs	40.47	37.82	36.20	34.71	33.56	32.57	31.62
CNN-DMRI	39.55	38.73	38.11	37.55	37.01	36.49	36.04
RED-WGAN	36.53	34.47	33.04	33.04	32.15	30.60	29.56
RicianNet	39.05	38.73	38.11	37.55	37.01	36.49	36.04
Proposed	**40.53**	**39.06**	**38.12**	**37.52**	**37.05**	**36.45**	**36.10**

Table 3: Brainweb T1-w MRI denoising performance measure in SSIM values with noise levels from 3% to 15%

Method	**Noise Levels**						
	3%	**5%**	**7%**	**9%**	**11%**	**13%**	**15%**
BM3D	0.933	0.893	0.834	0.786	0.727	0.703	0.689
CNLM	0.959	0.911	0.876	0.811	0.787	0.723	0.703
PRI-NLM3D	0.961	0.927	0.895	0.864	0.831	0.813	0.789
CNN3D	0.945	0.897	0.874	0.856	0.855	0.832	0.804
MCDnCNNg	0.953	0.930	0.911	0.879	0.856	0.811	0.793
MCDnCNNs	0.968	0.941	0.929	0.891	0.877	0.857	0.837
CNN-DMRI	0.959	0.950	0.940	0.931	0.923	0.912	0.904
RED-WGAN	0.945	0.896	0.874	0.856	0.855	0.815	0.820
RicianNet	0.827	0.821	0.818	0.815	0.815	0.813	0.812
Proposed	**0.987**	**0.978**	**0.969**	**0.961**	**0.955**	**0.946**	**0.938**

Table 4: IXI T1-w MRI dataset denoising performance measure in PSNR values with noise levels from 3% to 15%

Method	**Noise Levels**						
	3%	**5%**	**7%**	**9%**	**11%**	**13%**	**15%**
CNN-DMRI	38.38	37.40	36.56	35.83	35.18	34.58	34.07
CNN3D	38.46	35.86	33.61	32.79	31.49	29.91	28.69
PRI-NLM3D	38.39	37.28	36.84	33.18	32.40	31.87	31.07
MCDnCNNg	39.38	37.12	35.40	33.86	32.54	31.10	29.96
MCDnCNNs	40.47	37.82	36.20	34.71	33.56	32.57	31.62
RED-WGAN	36.53	34.47	33.04	33.00	32.15	30.60	29.56
Proposed	**39.92**	**38.34**	**36.88**	**36.05**	**35.33**	**34.42**	**33.52**

7.2 Bias correction results

The correction of bias field in the spatial intensity distribution improved the structural information, resulting in enhanced image quality. Figure 12 shows the performance evaluation of quantitative results of our methods, comparing them with other existing state-of-the-art techniques as well as shown in Table 6. We compared our method with other prominent bias correction methods such as N4ITK [78], CycleGAN [79], and inhomoNet

Journal of Information Systems Engineering and Management
2024, 9(4s)
e-ISSN: 2468-4376
https://www.jisem-journal.com/ **Research Article**

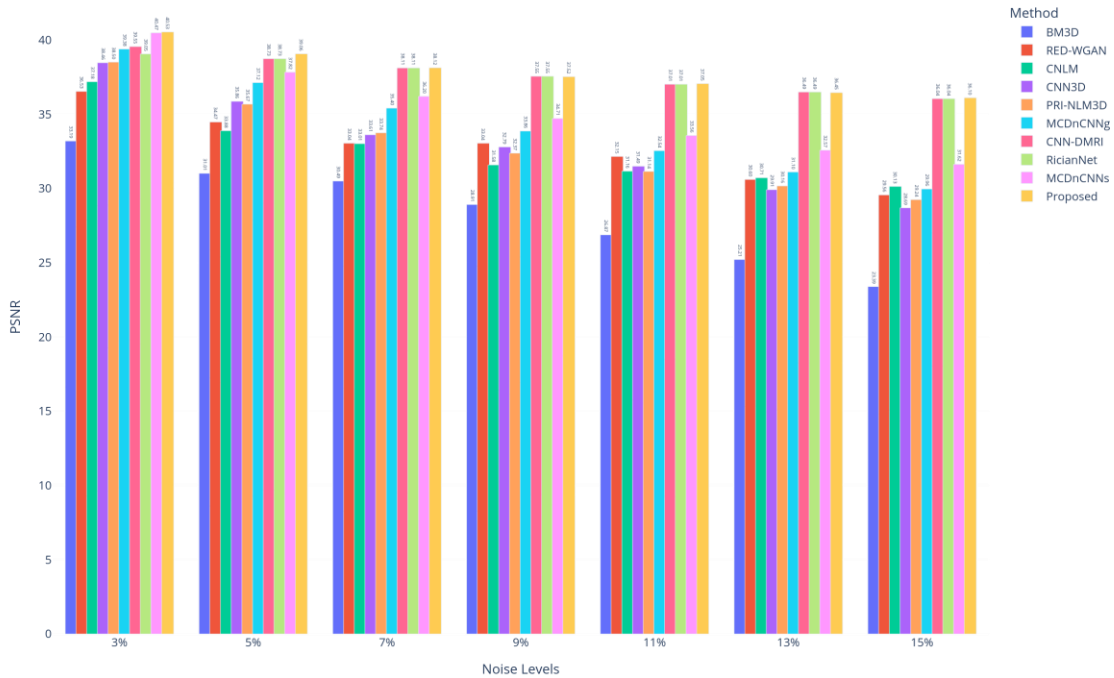

Figure 8: Noise levels vs PSNR results obtained with Brainweb T1-W MRI denoising evaluation

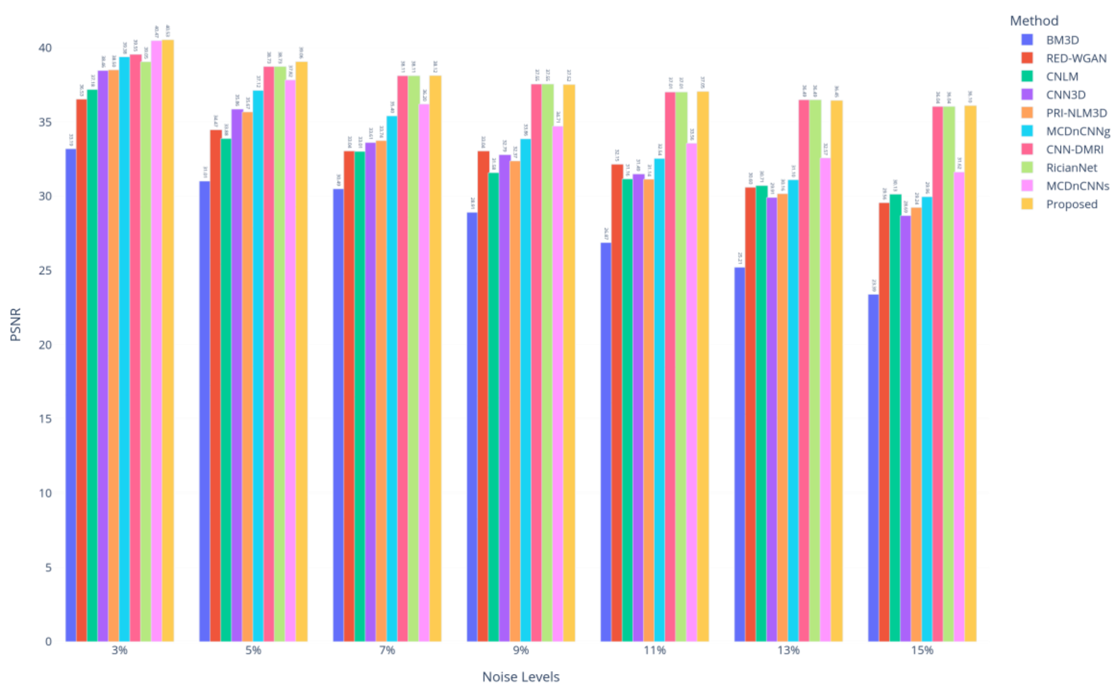

Figure 9: Noise levels vs PSNR results obtained with Brainweb T2-W MRI denoising evaluation

Journal of Information Systems Engineering and Management
2024, 9(4s)
e-ISSN: 2468-4376
https://www.jisem-journal.com/ **Research Article**

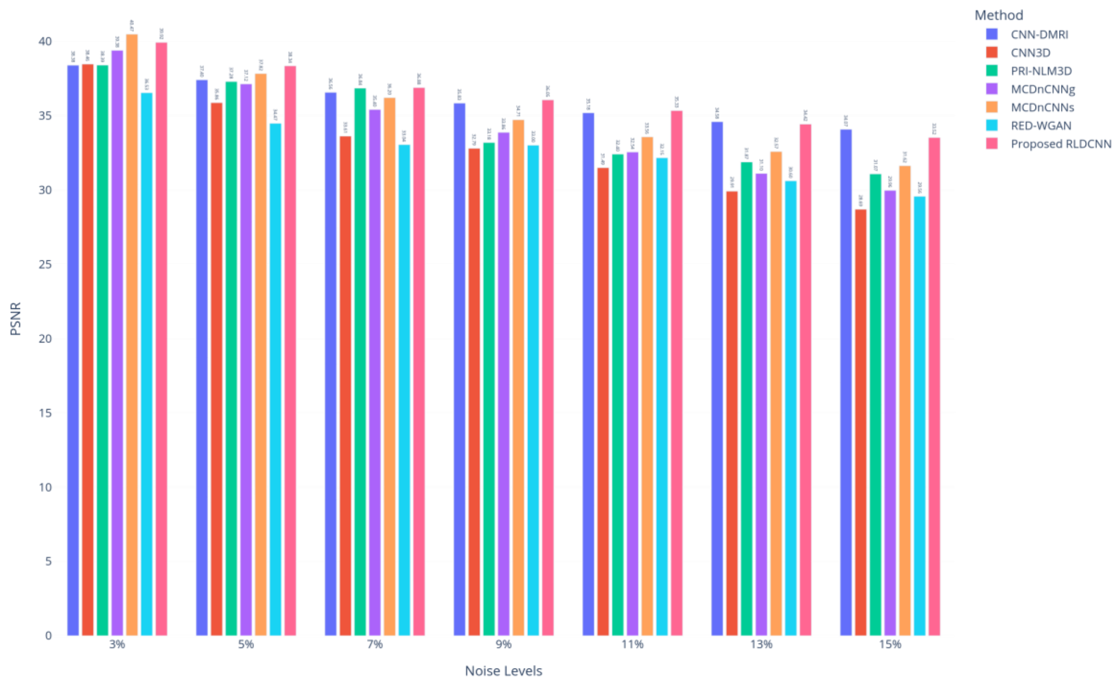

Figure 10: Noise levels vs PSNR results obtained with Brainweb PD-W MRI denoising evaluation

Table 5: IXI T1-w MRI dataset denoising performance measure in SSIM values with noise levels from 3% to 15%

Method	**Noise Levels**						
	3%	**5%**	**7%**	**9%**	**11%**	**13%**	**15%**
CNN-DMRI	0.762	0.750	0.736	0.729	0.720	0.718	0.713
CNN3D	0.954	0.929	0.909	0.900	0.893	0.866	0.853
PRINLM3D	0.966	0.927	0.894	0.864	0.837	0.794	0.789
MCDnCNNg	0.957	0.939	0.907	0.879	0.846	0.817	0.794
MCDnCNNs	0.966	0.937	0.928	0.893	0.876	0.857	0.839
RED-WGAN	0.969	0.937	0.928	0.899	0.878	0.859	0.841
Proposed	**0.988**	**0.981**	**0.976**	**0.969**	**0.959**	**0.948**	**0.933**

[60] to analyze the experimental outcomes. The numerical observations demonstrate that our proposed method outperforms existing bias correction methods. The quality of bias correction in MR images is measured using the MSE, PSNR, and SSIM metrics. The numerical analysis indicates that our proposed method shows better performance, very close to the target images. The bias-corrected results of T1-w MR images from the Brainweb and IXI datasets are displayed in Figure 12. Figures (a) and (b) show bias-affected images in the first column, ground-truth images in the middle column, and bias-corrected images in the third column, respectively.

Table 6 shows the quantitative analysis of experimental evaluations of bias correction results in PSNR and SSIM values of randomly selected images. The experimental assessment yielded an average PSNR of 34.00 and an SSIM of 0.974, significantly higher than the existing bias correction methods.

Table 7 shows the comparison of model performance evaluation with the existing state-of-the art bias-correction methods for MR images, and the Figure 11 depicts the same in pictorial form.

The guided L1 data loss regularizer helps to retain important feature maps in the generated images.

Journal of Information Systems Engineering and Management
2024, 9(4s)
e-ISSN: 2468-4376
https://www.jisem-journal.com/ Research Article

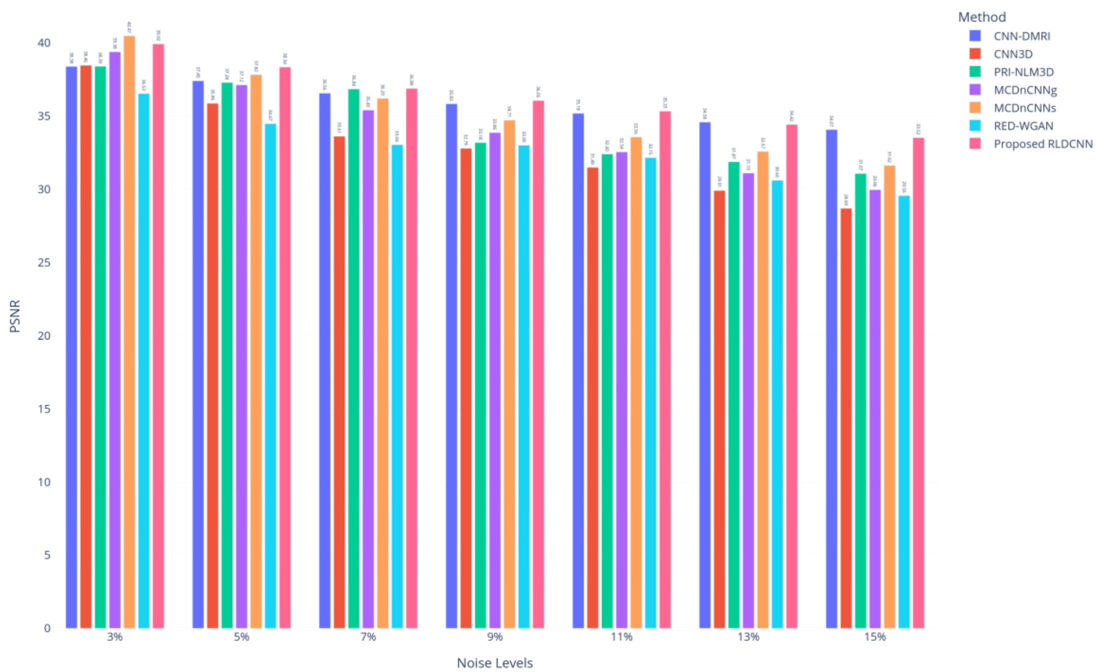

Figure 11: Noise levels vs PSNR results obtained with IXI T1-W MRI denoising evaluation

Table 6: Bias field correction results of randomly selected T1-w MRI slices in PSNR and SSIM values

MRI Slice No.	**PSNR**	**SSIM**	**MRI Slice No.**	**PSNR**	**SSIM**
Axial-56	30.46	0.938	Axial-61	31.03	0.952
Axial-63	30.91	0.953	Axial-90	36.59	0.990
Axial-67	30.21	0.956	Axial-85	36.53	0.990
Axial-69	30.90	0.957	Axial-92	36.81	0.990
Axial-73	31.24	0.958	Axial-87	36.41	0.990
Axial-77	30.56	0.966	Axial-98	36.75	0.990
Axial-79	31.56	0.966	Axial-84	36.33	0.990
Axial-80	36.53	0.988	Axial-99	36.84	0.990
Axial-83	36.18	0.990	Axial-102	36.88	0.990
Axial-58	30.52	0.944	Axial-97	36.80	0.990
Average:				**34.00**	**0.974**

The adversarial data loss is calculated by mapping and subtracting it from the ground-truth images, aiding in identifying and eliminating references. Histogram correlation mapping allows for image generation with better feature preservation by comparing the gray-level intensity values in the ground-truth pixels of reference images. The loss of information in 3D images provides accurate spatial intensity values in the restored images, thus restoring normalized image intensity values and achieving improved image results. Collectively, the loss of image information transmits necessary data to the image generator, thereby enhancing the overall

Journal of Information Systems Engineering and Management
2024, 9(4s)
e-ISSN: 2468-4376
https://www.jisem-journal.com/ **Research Article**

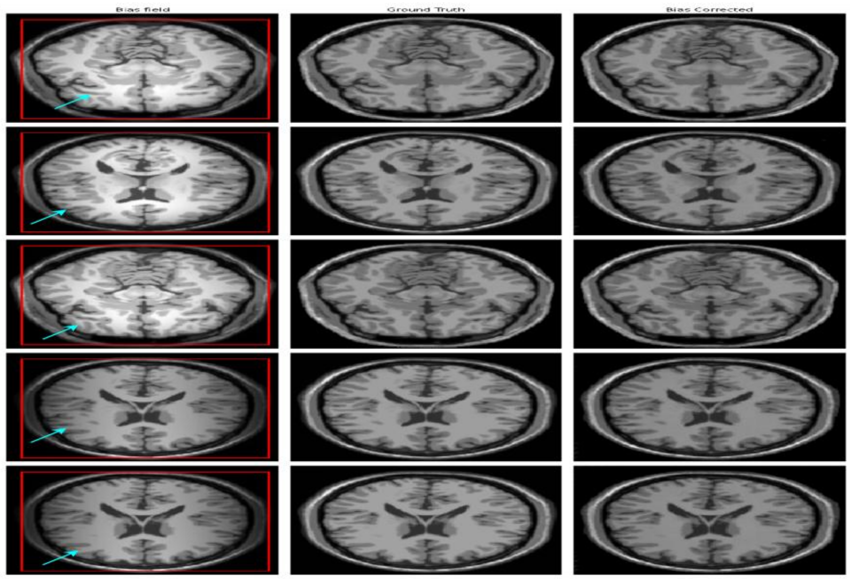

(a) Brainweb MRI bias correction

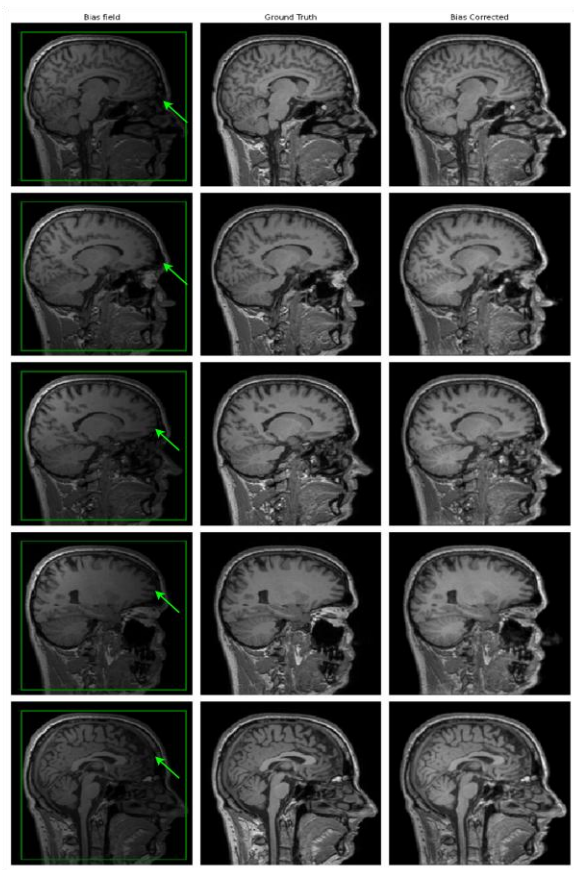

(b) IXI real MRI bias correction

Figure 12: Bias-field corrected simulated and real brain MR images

Journal of Information Systems Engineering and Management
2024, 9(4s)
e-ISSN: 2468-4376
https://www.jisem-journal.com/ **Research Article**

Table 7: Comparative analysis of averaged Bias field correction results in PSNR and SSIM values of randomly selected T1-w MRI slices

MRI Slice No.	**PSNR**	**SSIM**
Homomorphic [55]	18.8390	0.8216
N4ITK [78]	20.5950	0.9122
MICO [80]	22.6990	0.9127
C-GAN [79]	26.9470	0.9324
Pix2Pix [81]	26.1670	0.9324
Inhomo-Net [60]	29.1290	0.9515
Proposed RLDCNN	**34.0090**	**0.9740**

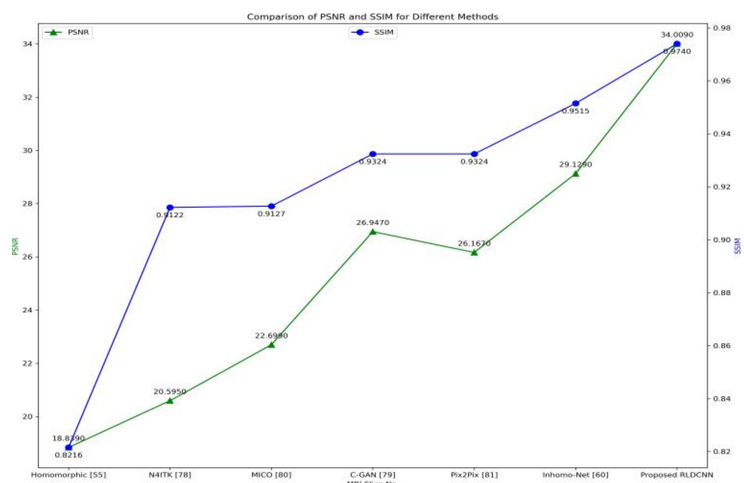

Figure 13: Comparative analysis of averaged PSNR and SSIM results with other existing bias correction methods

performance of the network model.

7.3 Discussion

The RLDCNN bias correction model effectively eliminates bias effects in generated images. Without dilation, the model produces overly smooth and blurred regions with less distinctive structural features. Adding skip-connection kernels improves image quality by transferring details from the encoder features to the decoder block. Furthermore, adding feature-aware and attention-oriented skip connections enhances image quality by accurately updating the intensity and location space of area-specific pixels. Computational complexity analysis indicates that each modification of a network model results in minimal changes in the model parameters. Skip connections do not affect the computational efficiency while achieving high measurement values and effectively transferring optimal information from the encoder to the decoder network.Preserving maximum image information during bias reduction eliminates data uncertainty, leading to effective segmentation operations. The proposed methodology offers a bias reduction method that does not require iterative regularization of empirical noise or bias parametric estimation using traditional methods. It applies gray-level

Journal of Information Systems Engineering and Management
2024, 9(4s)
e-ISSN: 2468-4376
https://www.jisem-journal.com/ Research Article

and spatial pixel information, adapting as a non-parametric method. Pixel-wise error field correction can lead to better segmentation using linear combinations of orthogonal basis functions. Furthermore, modeling spatial intensity levels, bias fields, and cluster intensity centers can be more effective when determining threshold criteria for cluster regions of pixels. A detailed experimental analysis of bias correction and image segmentation methods indicate that the proposed approaches for simulated and real brain MR images show promising results similar to those of other four modern bias correction methods.

8 Conclusion

This paper presents a deep learning-based random noise removal and bias-field effects correction in MR images that affect the original intensity information. Uniform noise effects distort the image contents, changing original pixel values, whereas bias-field changes the intensity distributions with smoothly varying levels across the spatial image regions. The noise and bias-field effects severely affect further downstream image processing tasks, including segmentation, object detection, and classification. This paper presents an RLDCNN model that consists of a deep residual learning network for noise removal and a generator-discriminator model for restoring enhanced quality MR images. The proposed models consider multi-level image information to extract the essential image features by representing different receptive fields. The attention-guided skip-connection dilated network module transmits optimal and contextual information between the encoder-decoder blocks. The proposed method provides essential image characteristic maps by localizing spatial details, structural information, and reallocation of pixel intensity. This methodology incorporates different types of information loss estimation, such as guided L1 loss, which helps to improve image reconstruction capabilities during data up-sampling. The histogram correlation match maintains uniform intensity levels in image regions affected by biases, and the 3D spatial loss estimate ensures the spatial location of the pixels in the restored image with desired intensity values. Different information loss estimation functions formulate robust and accurate strategies for recovering quality images by correcting intensity bias and non-uniformity estimation. The proposed bias correction scheme is based on supervised deep learning. Therefore, a fundamental ground truth MRI dataset is used as a reference to map the obtained results. This method can be extended further to unsupervised deep learning-based bias correction to consistently restore the expected level of uniform intensity distribution in soft tissue regions across regenerated images. In addition, this method may be used with real MRI datasets using self-learning with minimal image labels. During the deposition process, maintaining the main features of the map while reducing bias artifacts such as random noise, thermal noise, movement effects, and ghosting artifacts will improve image quality. A robust multiple artifacts removal method can be an effective preprocessing image analysis technique to improve overall MR image quality. A functionally sensitive and semantically driven image analysis model is needed to properly eliminate several image artifacts and enhance the reliability of computer methods in clinical image analysis applications for correct and accurate predictable results. The limitation of the present work is inadequate training with a minimal real clinical MRI dataset. It will be revised to make it a robust method for effective and reliable performance.

References

[1] *Osteoarthritis and Cartilage*, vol. 22, no. 10, pp. 1692 1702, 2014.

[2] S. Song, Y. Zheng, and Y. He, review of methods for bias correction in medical *Biomedical Engineering Review*, vol. 1, no. 1, 2017.

[3] E. N. Manson, S. Inkoom, and A. N. Mumuni, of magnetic field inhomogeneity on the quality of magnetic resonance images and compensation techniques: a *Reports in Medical Imaging*, pp. 43 56, 2022.

[4] shim technologies for ultra high field *Neuroimage*, vol. 168, pp. 59 70, 2018.

Journal of Information Systems Engineering and Management
2024, 9(4s)
e-ISSN: 2468-4376
https://www.jisem-journal.com/ **Research Article**

[5] *Analytical biochemistry*, vol. 529, pp. 17 29, 2017.

[6] t 2 magnetic resonance imaging in head phantom for radiotherapy treatment planning: Preliminary *Applied Magnetic Resonance*, vol. 51, pp. 59 69, 2020.

[7] -field mr diffusion-weighted image denoising *Journal of Magnetic Resonance Imaging*, vol. 50, no. 6, pp. 1937 1947, 2019.

[8] *Measurement Science Review*, vol. 13, no. 4, pp. 177 186, 2013.

[9] in *2008 9th International Conference on Signal Processing*, pp. 2154 2157, 2008.

[10] R. A. Haddad, A. N. Akansu, *et al.* *IEEE Transactions on Signal Processing*, vol. 39, no. 3, pp. 723 727, 1991.

[11] G. Papari, N. Idowu, and T. *IEEE Transactions on Image Processing*, vol. 26, no. 1, pp. 251 261, 2017.

[12] *Measurement Science and Technology*, vol. 22, no. 2, p. 025803, 2011.

[13] S. P. Awate and R. T. Whitaker, -preserving mri denoising: A nonparametric empirical bayes *IEEE Transactions on Medical Imaging*, vol. 26, no. 9, pp. 1242 1255, 2007.

[14] C. S. Anand and J. S. Sahambi, domain non-linear filtering for mri *Magnetic Resonance Imaging*, vol. 28, no. 6, pp. 842 861, 2010.

[15] S. Anila, S. Sivaraju, and N. Devarajan, new contourlet based multiresolution approximation for *National Academy Science Letters*, vol. 40, pp. 39 41, 2017.

[16] X. Zhang, Z. Xu, N. Jia, W. Yang, Q. Feng, W. Chen, and Y. Feng, of 3d magnetic resonance images by using higher-order singular value *Medical image analysis*, vol. 19, no. 1, pp. 75 86, 2015.

[17] A. Buades, B. Coll, and J.-M. Morel, image sequences does not require motion in *IEEE Conference on Advanced Video and Signal Based Surveillance, 2005.*, pp. 70 74, IEEE, 2005.

[18] J. V. Manjón, J. Carbonell- - - denoising using non-local *Medical image analysis*, vol. 12, no. 4, pp. 514 523, 2008.

[19] J. V. Manjón, P. Coup´e, A. Buades, V. Fonov, D. L. Collins, and M. Robles, -local mri *Medical image analysis*, vol. 14, no. 6, pp. 784 792, 2010.

[20] J. V. Manjón, P. Coup´e, and A. Buades, noise estimation and denoising using non-local *Medical image analysis*, vol. 22, no. 1, pp. 35 47, 2015.

[21] J. V. Manjón, - -local means denoising of mr images with spatially varying noise *Journal of Magnetic Resonance Imaging*, vol. 31, no. 1, pp. 192 203, 2010.

[22] *International conference on medical image computing and computer-assisted intervention*, pp. 33 40, Springer, 2006.

[23] - *Magnetic Resonance Imaging*, vol. 34, no. 7, pp. 990 999, 2016.

Journal of Information Systems Engineering and Management
2024, 9(4s)
e-ISSN: 2468-4376
https://www.jisem-journal.com/ **Research Article**

[24] -local means filter for 3d mr image denoising iet image *Institution of Engineering and Technology*, 2011.

[25] G. Chen, P. Zhang, Y. Wu, D. Shen, and P.- collaborative non-local *Neurocomputing*, vol. 177, pp. 215 227, 2016.

[26] -dmri: a convolutional neural network for denoising of magnetic reso- *Pattern Recognition Letters*, vol. 135, pp. 57 63, 2020.

[27] An unsupervised mr image denoising network with deep image *Theoretical Computer Science*, vol. 880, pp. 97 110, 2021.

[28] L. Wu, S. Hu, and C. Liu, images with parallel residual learning of con- *Computational Intelligence and Neuroscience*, vol. 2021, no. 1, p. 5577956, 2021.

[29] Learning image restoration without clean in *International Conference on Machine Learning*, pp. 2965 2974, PMLR, 2018.

[30] *Neural Processing Letters*, vol. 55, no. 6, pp. 7807 7850, 2023.

[31] K. Zhang, W. Zuo, Y. Chen, D. Meng, and L. Zhang, a gaussian denoiser: Residual learning of deep cnn for image *IEEE Transactions on Image Processing*, vol. 26, no. 7, pp. 3142 3155, 2017.

[32] M. E. Brain, S. Amukotuwa, and R. Bammer, learning denoising reconstruction enables faster t2- *Journal of Medical Imaging and Radiation Oncology*, 2024.

[33] : Self-supervised diffusion mri denoising with generative diffusion *arXiv preprint arXiv:2302.03018*, 2023.

[34] diffusion probabilistic *European Journal of Nuclear Medicine and Molecular Imaging*, vol. 51, no. 2, pp. 358 368, 2024.

[35] Y. Zhu, K. Zhang, J. Liang, J. Cao, B. Wen, R. Timofte, and L. Van Gool, diffusion models for plug-and-play image in *Proceedings of the IEEE/CVF Conference on Computer Vision and Pattern Recognition*, pp. 1219 1229, 2023.

[36] - tions, and measurement units for mri in radiation *Medical physics*, vol. 47, no. 9, pp. 4101 4114, 2020.

[37] Y. Chang, Z. Li, G. Saju, H. Mao, and T. Liu, learning-based rigid motion correction for magnetic resonance imaging: A *Meta-Radiology*, p. 100001, 2023.

[38] J. Sled, A. Zijdenbos, and A. Evans, nonparametric method for automatic correction of intensity *IEEE Transactions on Medical Imaging*, vol. 17, no. 1, pp. 87 97, 1998.

[39] J. V. Manjón, J. J. Lull, J. Carbonell-Ca L. - and M. Robles, nonparametric mri inhomogeneity corr *cal image analysis*, vol. 11, no. 4, pp. 336 345, 2007.

[40] S. Viswanath, D. Palumbo, J. Chappelow, P. Patel, B. N. Bloch, N. Rofsky, R. Lenkinski, E. Genega, and A. evaluation of bias field correction algorithms for computer-aided detection of *Medical Imaging 2011: Computer-Aided Diagnosis*, vol. 7963, pp. 254 265, SPIE, 2011.

[41] L. J. Isaksson, S. Raimondi, F. Botta, M. Pepa, S. G. Gugliandolo, S. P. De Angelis, G. Marvaso, G. Petralia, O. De Cobelli, S. Gandini, *et al.* *Physica Medica*, vol. 71, pp. 7 13, 2020.

[42] E. Scalco, A. Belfatto, A. Mastropietro, T. Rancati, B. Avuzzi, A. Messina, R. Valdagni, and G. Rizzo, -mri signal normalization affects radiomics features *Medical physics*, vol. 47, no. 4, pp. 1680 1691, 2020.

[43] A. Madabhushi and J. K. correction in mr image *IEEE Transactions on Medical Imaging*, vol. 24, no. 5, pp. 561 576, 2005.

[44] -noise and bias- *IEEE Access*, vol. 8, pp. 98548 98561, 2020.

[45] -iterative multi-scale approach for intensity *Magnetic resonance imaging*, vol. 42, pp. 43 59, 2017.

[46] *IEEE Transactions on Medical Imaging*, vol. 26, no. 3, pp. 405 421, 2007.

[47] J. B. Arnold, J.-S. Liow, K. A. Schaper, J. J. Stern, J. G. Sled, D. W. Shattuck, A. J. Worth, M. S. Cohen, R. M. Leahy, J. C. Mazziotta, *et al.* *NeuroImage*, vol. 13, no. 5, pp. 931 943, 2001.

[48] S. Leger, S. Löck, V. Hietschold, R. Haase, H. J. Böhme, model for automatic correction of intensity non-uniformity in magnetic resonance *Physics and Imaging in Radiation Oncology*, vol. 4, pp. 32 38, 2017.

[49] Z. Y. Chua, W. Zheng, M. W. Chee, and V. *Journal of Magnetic Resonance Imaging: An Official Journal of the International Society for Magnetic Resonance in Medicine*, vol. 29, no. 6, pp. 1271 1279, 2009.

[50] Y. - *Cancers*, vol. 13, no. 12, p. 3000, 2021.

[51] *Journal of applied clinical medical physics*, vol. 21, no. 1, pp. 179 190, 2020.

[52] W. Wells, W. Grimson, R. Kikinis, and F. *IEEE Transactions on Medical Imaging*, vol. 15, no. 4, pp. 429 442, 1996.

[53] -preserved intensity inhomogeneity *Signal, Image and Video Processing*, vol. 12, pp. 791 798, 2018.

[54] neural in *Proceedings of the ISMRM Scientific Meeting & Exhibition, Paris*, vol. 1174, 2018.

[55] Y. Lee, Z. Wang, and Y.- - rection of mr *IFAC Proceedings Volumes*, vol. 36, no. 15, pp. 119 122, 2003.

[56] - mogeneity correction in brain mr *Computer Methods in Biomechanics and Biomedical Engineering: Imaging & Visualization*, 2019.

[57] of diffusion- *Journal of Medical and Biological Engineering*, vol. 37, pp. 508 518, 2017.

Journal of Information Systems Engineering and Management
2024, 9(4s)
e-ISSN: 2468-4376
https://www.jisem-journal.com/ **Research Article**

[58] L.-C. Chen, Y. Zhu, G. Papandreou, F. Schroff, and H. -decoder with atrous separable *Proceedings of the European conference on computer vision (ECCV)*, pp. 801 818, 2018.

[59] field and reconstructing uniform mri image by deep *Journal of Magnetic Resonance*, vol. 343, p. 107301, 2022.

[60] *Computerized Medical Imaging and Graphics*, vol. 84, p. 101748, 2020.

[61] -based brain malignant neoplasm classification using mri image segmentation assisted by bias field correction and histogram in *Brain Tumor MRI Image Segmentation Using Deep Learning Techniques*, pp. 135 161, Elsevier, 2022.

[62] L. Vinas, A. A. Amini, J. Fischer, and A. Sudhyadhom, multisequence mr bias correction *arXiv preprint arXiv:2209.13619*, 2022.

[63] *Biomedical Signal Processing and Control*, vol. 69, p. 102737, 2021.

[64] S. Boyd, N. Parikh, E. Chu, B. Peleato, J. Eckstein, *et al.* *Foundations and Trends in Machine learning*, vol. 3, no. 1, pp. 1 122, 2011.

[65] *arXiv preprint arXiv:2403.08162*, 2024.

[66] -and-play admm for image restoration: Fixed-point convergence and *IEEE Transactions on Computational Imaging*, vol. 3, no. 1, pp. 84 98, 2017.

[67] Y. Nesterov, of coordinate descent methods on huge-scale optimization *SIAM Journal on Optimization*, vol. 22, no. 2, pp. 341 362, 2012.

[68] R. Sun, Z.-Q. Luo, and Y. *Mathematics of Operations Research*, vol. 45, no. 1, pp. 233 271, 2020.

[69] *Neurocomputing*, vol. 345, pp. 67 76, 2019.

[70] X. Zhang, W. Yang, Y. Hu, and J. Dual-domain multi-scale convolutional neural network *2018 25th IEEE international conference on image processing (icip)*, pp. 390 394, IEEE, 2018.

[71] - *arXiv preprint arXiv:1511.07122*, 2015.

[72] semantic in *2018 IEEE winter conference on applications of computer vision (WACV)*, pp. 1451 1460, Ieee, 2018.

[73] C. Tan, J. Zhu, and P. scale super-resolution for brain mri in *IFIP International Conference on Artificial Intelligence Applications and Innovations*, pp. 165 176, Springer, 2020.

[74] -contrast mri super-resolution: Rectangle-window cross-attention transformer and arbitrary-scale up- *Proceedings of the IEEE/CVF International Conference on Computer Vision*, pp. 21230 21240, 2023.

[75] An interpretable network for multi-contrast mri image super-resolution *Computers in Biology and Medicine*, vol. 167, p. 107605, 2023.

[76] X. Mao, Q. Li, H. Xie, R. Y. *IEEE Transactions on Pattern Analysis and Machine Intelligence*, vol. 41, no. 12, pp. 2947 2960, 2019.

[77] I. Imperial College London, *IXI-Dataset*, 2024.

[78] N. J. Tustison, B. B. Avants, P. A. Cook, Y. Zheng, A. Egan, P. A. Yushkevich, and J. *IEEE Transactions on Medical Imaging*, vol. 29, no. 6, pp. 1310 1320, 2010.

[79] J.- -to-image translation using cycle- *Proceedings of the IEEE international conference on computer vision*, pp. 2223 2232, 2017.

[80] *Magnetic resonance imaging*, vol. 32, no. 7, pp. 913 923, 2014.

[81] P. Isola, J.- -to-image translation with conditional adversarial in *Proceedings of the IEEE conference on computer vision and pattern recognition*, pp. 1125 1134, 2017.